

REVIEW

Electron Affinities in the Periodic Table and an Example for As

Shuaiting Yan, Yuzhu Lu, Rui Zhang, Chuangang Ning*

Department of Physics, State Key Laboratory of Low Dimensional Quantum Physics, Frontier Science Center for Quantum Information, Tsinghua University, Beijing 100084, China

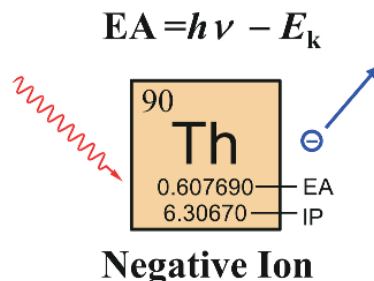
(Dated: Received on July 27, 2023; Accepted on September 5, 2023)

Based on our previous analysis of electron affinities of atoms and structures of atomic negative ions [J. Phys. Chem. Ref. Data **51**, 021502 (2022)], this review provides a concise presentation of the electron affinities of atoms. We briefly describe and compare three commonly used experimental methods for determining electron affinities to highlight their respective advantages and disadvantages. To illustrate the features of the slow electron velocity-map imaging method utilized in our current study, we conducted measurements on the electron affinity of As and excited states of its anion. The electron affinity of As was determined to be $6488.61(5) \text{ cm}^{-1}$ or $0.804485(6) \text{ eV}$. The fine structures of As^- were well resolved, with values of $1029.94(18) \text{ cm}^{-1}$ or $0.12770(3) \text{ eV}$ for 3P_1 and $1343.04(55) \text{ cm}^{-1}$ or $0.16652(7) \text{ eV}$ for 3P_0 above the ground state 3P_2 , respectively.

Key words: Periodic table, Electron affinity, Arsenic, Slow-electron velocity-map imaging

I. INTRODUCTION

The electron affinity (EA) is a fundamental parameter of an atom, defined as the amount of energy released when an electron is added to a neutral atom. It is a measurement of the capability of an atom to form the corresponding negative ion contrasting with the ionization potential (IP) which measures the difficulty to remove an electron from an atom. Both IP and EA are important for understanding chemical reaction and chemical properties. The electronegativity of an atom (χ) is defined as $\chi = (\text{IP} + \text{EA})/2$, and the hardness (η) is calculated as $\eta = \text{IP} - \text{EA}$ [1–6]. These values can be used to derive the bonding energy of a molecule in different charged states. For instance, if the bonding energy (E_b) of a molecule AB for the dissociation channel $\text{AB} \rightarrow \text{A} + \text{B}$ is known, the bonding energy E_b' of AB^- for



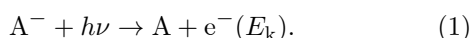
the channel $\text{AB}^- \rightarrow \text{A}^- + \text{B}$ can be deduced using the formula: $E_b' = E_b + \text{EA}(\text{AB}) - \text{EA}(\text{A})$ [1]. In the late 20th century, we had a good understanding of the negative ion properties of main-group elements. However, our knowledge about the atomic negative ions of transition elements, lanthanide, and actinides was limited or mostly qualitative due to the complex electronic structures arising from partially occupied d or f orbitals. Traditional experimental methods, like the laser photodetachment threshold (LPT) [3] and the laser photodetachment microscopy (LPM) [7] were inadequate for resolving the congested photodetachment channels. To overcome this challenge, we introduced the slow electron velocity-map imaging method (SEVI). With SEVI, we have accurately measured the EA values of most transitional elements and part of lanthanides and actinides. Previous review has provided a comprehensive summary of the historical background and the recent progress [8], which we will not repeat here. Instead, we present the EA value for each element in the periodic table in a concise format, aiming to provide conve-

* Author to whom correspondence should be addressed. E-mail: ningcg@tsinghua.edu.cn

nience for general readers. Furthermore, this work seeks to compare the three main experimental methods used to measure EA values of elements.

Another motivation of this study is to improve the accuracy of EA value of arsenic (As, $Z=33$). Arsenic is the only nonradioactive element in the p-block of the periodic table with an uncertainty of EA value as large as 1.7 cm^{-1} [8, 9]. The current value for EA(As) was reported as $6491.1(17) \text{ cm}^{-1}$ or $0.8048(2) \text{ eV}$. Furthermore, As^- has two excited states, namely 3P_1 and 3P_0 . The energies of these excited states have been determined using the LPT method. The energy level for 3P_1 was measured to be $1029.2(16) \text{ cm}^{-1}$, while $1325.2(81) \text{ cm}^{-1}$ for 3P_0 above the ground state 3P_2 [9]. Notably, the uncertainties associated with these energy measurements are significantly larger compared to the same group elements, such as phosphorus (P) [10], antimony (Sb) [11], and bismuth (Bi) [12]. Given the relatively larger uncertainties and importance of accurate EA values, it is crucial to conduct a new measurement to improve the accuracy of arsenic's electron affinity.

The EA value of an atom A is determined by the difference in the total energies between the ground states of A and its negative ion A^- [3]. Accurate experimental EA values are primarily obtained through the powerful photoelectron spectroscopy technique. In a typical photodetachment experiment, a narrow-linewidth laser beam intersects with a well-collimated anion beam. This results in the detachment of the extra electron from A^- , which can be observed from either the neutral atom A or the photoelectron e^- , depending on the specific experimental setup. This process can be represented as



Here, $h\nu$ represents the photon energy and E_k represents the kinetic energy of the outgoing photoelectron. The difference between the photon energy $h\nu$ and the kinetic energy E_k is referred to as the binding energy (BE) of the specific photodetachment channel:

$$\text{BE}(\text{A}_i^- \rightarrow \text{A}_f) = h\nu - E_k. \quad (2)$$

Here A_i^- represents A^- at its state i, and A_f for the neutral A at its state f. If both states i and f are their ground states, BE is equal to EA. However, in a photodetachment, the initial state of A^- and the final state of A may not be their ground states. For example, A^-

may be at its metastable state i, and the final neutral atom A may be at an excited state f. Since the energy levels of a neutral atom is well-known with a high accuracy, any photodetachment channel from the ground state of A^- can be used to measure the EA value without limitation to the final ground state. If an atom cannot form a stable negative ion, its EA is less than zero. For example, $\text{EA}(\text{He}) < 0$. It should be pointed out that He^- can form a metastable state $1s2s2p \ ^4P_{j=1/2, 3/2, 5/2}$, which is well above the photodetachment continuum limit [13–22]. This metastable state can decay into $\text{He} (^1\text{S}_0) + e^-$ via autodetachment through spin-orbital and spin-spin interaction [23].

II. EXPERIMENTAL METHODS

The experimental determination of atomic EA values primarily relies on the photoelectric effect. The first step of the experiment is to generate a sufficiently strong negative ion beam. Various types of ion sources are employed for EA measurements, including the gas discharge, the electrospray ionization, the laser ablation, and the cesium ion sputtering ion sources [24, 25]. The atoms with a high EA value can form negative ions easily. It is readily to generate a strong negative ion beam for these elements such as H^- , C^- , O^- , F^- , Cu^- . However, generating atomic anions of the elements with a very low EA value poses a significant practical challenge and remains a primary hurdle in these experiments. To overcome this challenge, some of them can be generated via the double charge exchange of the positive ion beam in an alkali vapor cell, such as Ca^- , Sr^- [26, 27]. Notably, we have successfully generated atomic anions of most of transitional elements [28–38], and part of lanthanides using the laser ablation ion source [39–42]. Recently, we have been able to produce atomic anions for two nonradioactive actinides, Th and U [43–45].

To determine the EA value as accurate as possible, photodetachment experiments are typically conducted near the photodetachment threshold [46, 47]. The photoelectron yield near the threshold can be predicted using the Wigner threshold law, which is represented by the following equation [48]:

$$\sigma_{\text{tot}} = \begin{cases} \alpha(h\nu - \text{BE})^{l+1/2}, & h\nu > \text{BE} \\ 0, & h\nu \leq \text{BE} \end{cases} \quad (3)$$

In this equation, σ_{tot} is the total single-photon detach-

ment cross section, BE is the binding energy of the photodetachment channel, l is the orbital angular momentum of outgoing photoelectrons, and α is a constant. For an s subshell electron, the outgoing photoelectron has a p-wave ($l=1$) due to the angular momentum \hbar of each photon carrier. In the case of a p electron, there are two possible partial waves: s-wave ($l=0$) and d-wave ($l=2$). However, the contribution of the d-wave is negligible near the threshold. Similarly, for photodetaching a d electron near the threshold, only the p-wave is observable. In a typical LPT experiment, the yield of photoelectrons and the neutral atoms were monitored by scanning the photon energy around the photodetachment threshold. Then, the threshold was obtained by fitting the experimental data using Eq.(3). As shown in FIG. 1, the s-wave has a very sharp onset as $h\nu$ exceeds BE, particularly at the zero baseline. Therefore, the LPT method can determine the EA value very accurately by scanning the photon energy if it is an s-wave photodetachment [3, 49]. However, this method becomes less precise for a p-wave photodetachment due to a zero-slope onset, especially when multiple photodetachment channels have very small energy gaps between them. For example, in FIG. 1(b), it is difficult to distinguish the three p-wave channels with thresholds located at 10000, 10010, and 10020 cm^{-1} respectively. The LPT method may prove optimistic for the error bars if unknown baselines or non-Wigner threshold effects alter the behavior predicted by Eq.(3). The presence of nonconstant background counts contributed from either the excited states of the negative ion or other species with the same mass may significantly affect the EA measurement. It should be pointed out that the cross-section for p-wave photodetachment is usually much smaller than that for an s-wave near the threshold. The cross section of p-wave photodetachment is usually one order of magnitude lower than that of s-wave at $E_k \approx 100 \text{ cm}^{-1}$, and three orders of magnitude lower at $E_k \approx 1 \text{ cm}^{-1}$. This is why the LPT method is predominantly used to measure EA values of main-group elements. For the transitional elements, whose outer valence electrons occupy either d or s subshell, only the p-wave is observable near the threshold. The congested photodetachment channels resulting from fine-structure splitting and the very low p-wave photodetachment cross section make the LPT method unsuitable for measuring the EA values of transitional elements.

Another experimental method used to measure EA

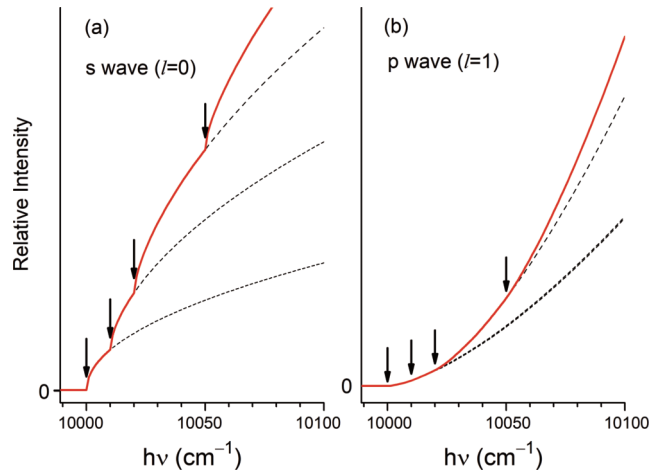


FIG. 1 Simulated threshold behaviors of s-wave and p-wave photodetachment according to the Wigner threshold law. The arrows indicated four photodetachment channels with thresholds located at 10000, 10010, 10020, and 10050 cm^{-1} , respectively.

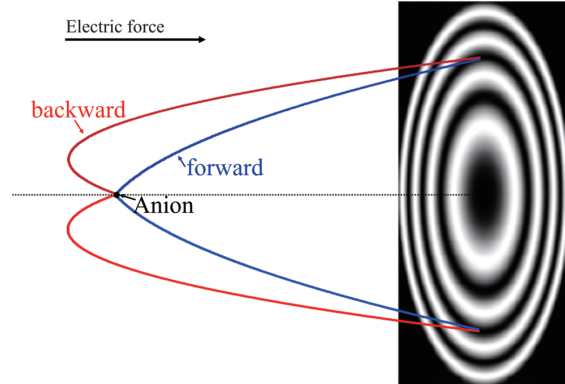


FIG. 2 Scheme of the laser photodetachment microscopy (LPM). The concentric bright and dark rings are the interference results between the forward and backward ways of photoelectrons.

values of atoms is the LPM method [7, 50–54]. In this method, the kinetic energy of photoelectrons is determined via measuring their de Broglie wavelength λ_d . As shown in FIG. 2, a low-energy photoelectron travels in a uniform electric field, following a parabolic trajectory similar to a free fall. Any point on the detector within the electron's reach has two possible ways for the photoelectron to travel towards it. The interference between two ways results in a pattern of concentric bright and dark rings. By analyzing this interference pattern, the de Broglie wavelength λ_d of photoelectrons can be obtained. The kinetic energy of photoelectrons is given by $E_k = h^2 / (2m_e \lambda_d^2)$, where m_e is the mass of an electron. In a typical LPM experiment, the uniform electric field was generated by applying potentials to a few dozens of parallel plates. The negative ions were pho-

todetached in the uniform electric field, and the hitting positions of outgoing photoelectrons were recorded using a charge-coupled-device (CCD) camera. The interference pattern was obtained by accumulating thousands of laser shots. To observe a clear interference pattern, the kinetic energy of photoelectrons is usually kept below 0.1 meV. Only s-wave photodetachment exhibits an observable photoelectron yield at such low kinetic energy. Thus, the LPM method has proven to acquire the most accurate EA values so far, typically with a 1- μ eV uncertainty. However, this method is limited to the main-group elements.

Our group utilizes the velocity-map imaging (VMI) method to accurately measure the kinetic energy of photoelectrons [55]. In this method, a set of electrostatic lens accelerates photoelectrons toward a 2D position-sensitive detector. Photoelectrons with the same kinetic energy form a spherical shell, which appears as a circle when being projected onto the VMI screen. The radius of the circle is directly proportional to the velocity of photoelectrons. The VMI method offers an excellent energy resolution for low-energy electrons due to its insensitivity to the residual electromagnetic fields in the environment. For slow photoelectrons with kinetic energy of a few meV, the size of spherical shell is only a few millimeters. While stray fields may shift the position of the spherical shell globally, they do not distort its shape. Additionally, the short time of flight of photoelectrons, as they are accelerated to a few hundred of eV by the VMI lens voltage before hitting the phosphor screen, minimizes the impact of stray fields on their trajectories. This stands in contrast to conventional spectrometers based on hemispherical electrostatic energy analyzers or the magnetic bottles, which exhibit a poor energy resolution for very slow electrons. A specialized VMI technique called the slow electron velocity-map imaging (SEVI) method has been developed recently [56–58]. The underlying principle of SEVI is straightforward: if the relative energy resolution $\Delta E/E$ remains constant, the absolute energy resolution ΔE improves as the kinetic energy E decreases. SEVI typically achieves a $\Delta E/E$ of 2%, resulting in an energy resolution ΔE of 0.2 meV for $E=10$ meV. An energy resolution of better than 0.1 meV has been reported [59]. This high resolution, typically a few cm^{-1} , for example, is crucial for measuring EAs of the transitional elements, as it allows for the resolution of fine structures. Notably, for p-wave photodetachment, the cross-section of SEVI with

$E_k \approx 100 \text{ cm}^{-1}$ is significantly higher compared to that of LPT or LPM with $E_k \approx 1 \text{ cm}^{-1}$ [8].

FIG. 3 depicts the schematic diagram of our Cryo-SEVI apparatus, which is our second-generation spectrometer. The key difference between this and our first-generation spectrometer lies in the addition of a cryogenically controlled ion trap. For a more detailed descriptions of our spectrometer, please refer to our previous work [29, 35]. In summary, it consists of four main components: the laser ablation ion source, the cryogenically controlled ion trap, the time-of-flight (TOF) mass spectrometer, and the SEVI spectrometer. To generate negative ions, a 532-nm Nd:YAG pulsed laser is focused onto a translating and rotating metal disk. These negative ions are then accumulated in an octupole radio-frequency (rf) ion trap. The ion trap is mounted on a cryogenic refrigerator with a controllable temperature within the range 5–300 K. Typically, the negative ions are stored in the trap for 45 ms to ensure sufficient collisions with the buffer gas. A mixture of 20% H₂ and 80% He is frequently used as the buffer gas. The cold ion trap proves highly advantageous in enhancing the ion beam intensity, identifying excited states, and reducing the interference from molecular anions with the same mass as atomic anions. The cooled ions are ejected via pulsed potentials applied on the end caps and subsequently analyzed by the TOF mass spectrometer [60, 61]. Ions of interest are photodetached using a tunable laser in the interaction zone of the VMI system. The resulting photoelectrons are projected onto a microchannel-plate enhanced phosphor screen by the electric field of the VMI lens. A charge-coupled-device (CCD) camera is employed to measure the position where the electron hits. Generally, each photoelectron usually triggers around one dozen pixels, and the weighted center of each hit is recorded in an event-count mode. This allows the imaging system to achieve a position resolution beyond the size of the CCD pixel. An image is usually an accumulation of 50000 laser shots. The machine operates at a repletion rate of 20 Hz. In our current work, a tunable dye laser with a linewidth of 0.06 cm^{-1} serves as the photodetachment laser. Its wavelength is monitored by a HighFine WS6-600 wavelength meter with an accuracy of 0.02 cm^{-1} .

In a typical SEVI experiment, the negative ion is photodetached using a linear polarized laser with a polarization parallel to the phosphor screen. The resulting photoelectron angular distribution (PAD) is described by the following equation [62–68]:

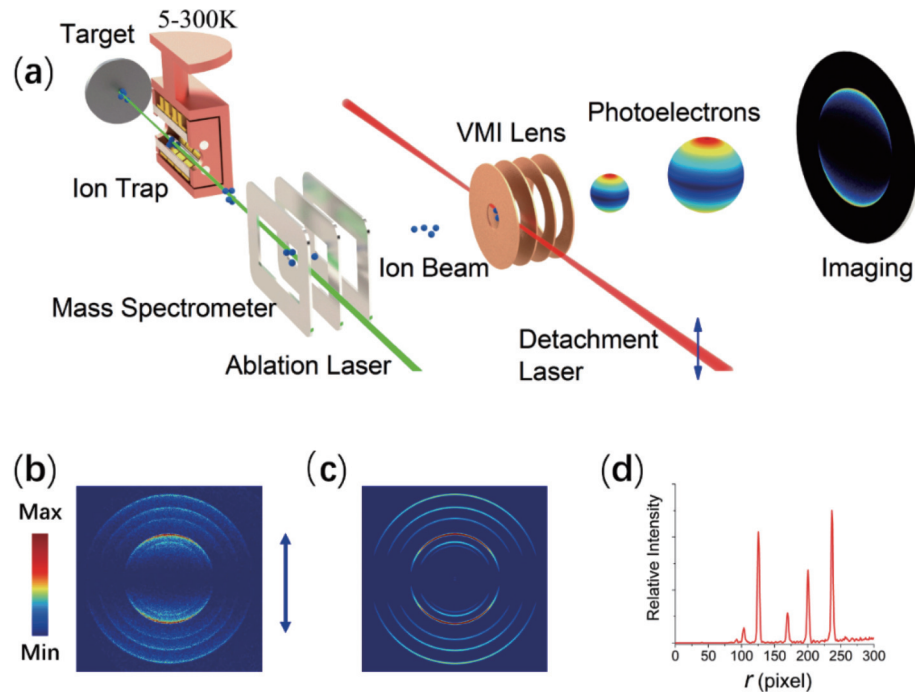


FIG. 3 (a) Schematic diagram of the Cryo-SEVI apparatus at Tsinghua University. One typical raw image from the projected photoelectron shells (b), the reconstructed image (c), and the velocity spectrum (d). The double-headed arrows indicate the laser polarization.

$$\frac{d\sigma}{d\Omega} = \frac{\sigma_{\text{tot}}}{4\pi} [1 + \beta P_2(\cos\theta)], \quad (4)$$

where Ω is the solid angle, $P_2(\cos\theta)$ is the second-order Legendre polynomial, $(3\cos^2\theta - 1)/2$, θ is the angle between the velocity of the emitted photoelectron and the electric field of the laser, and β (varies from -1 to 2) is the anisotropy parameter. The value of β depends on the kinetic energy of photoelectrons and the symmetry of the electronic state. Measuring value of β proves beneficial in assigning the electronic state. The distribution of outgoing photoelectrons exhibits a cylindrical symmetry. As a result, the 3D photoelectron distribution can be reconstructed from the projected 2D image using either an inverse Abel transformation [69, 70] or the maximum entropy velocity Legendre reconstruction (MEVELER) method [71, 72]. We often use the MEVELER method as it avoids the central-noise issue.

Table I compares the characteristics of three experimental methods: LPT, LPM, and SEVI. Both LPT and LPM methods measure the EA value near the threshold, requiring prior knowledge of the EA value. In contrast, SEVI offers a large dynamic range of the kinetic energy, typically a few eV. SEVI can initially obtain an approximate EA value for an element with an unknown EA value through a preliminary measurement, and then further enhance the accuracy by selecting a specific

photodetachment channel. In contrast to LPT and LPM, which operate near the threshold, SEVI allows measurements at higher kinetic energies, around $E_k \approx 10$ meV. This higher energy range results in a significantly higher count rate, thanks to the Wigner threshold law. This is a very important advantage for a p-wave photodetachment.

It should be pointed out that the LPT method requires scanning the photon energy and measuring the relative intensity of photoelectrons or neutral atoms. It is necessary to accurately measure the intensities of the laser beam and the ion beam, while maintaining stable overlap between two beams. On the other hand, LPM and Cryo-SEVI only require the measurement of photoelectron intensity. LPT relies on the Wigner threshold law and therefore is sensitive to unknown non-zero baselines and non-Wigner effects. If certain systemic errors are estimated incorrectly, it may underestimate the measurement uncertainty. We have observed significant deviation in the energy levels of Co⁻ [33], Ir⁻ [38], and Os⁻ [73, 74] reported by the LPT method.

III. RESULTS AND DISCUSSION

In FIG. 4, the photoelectron image and binding energy spectra of As⁻ are presented at a photon energy of $h\nu = 17407$ cm⁻¹ using a dye laser (Spectra-Physics,

TABLE I Comparison of three different experimental methods (laser photodetachment threshold, LPT; laser photodetachment microscopy, LPM; cryogenic ion trap slow-electron velocity-map imaging, Cryo-SEVI) used for EA measurements.

Characteristics	LPT	LPM	Cryo-SEVI																																																																																																																																
Resolving power (two adjacent transitions)	Overlapped spectrum, excellent resolution for s-wave, but poor for p-wave.	Overlapped interference patterns, only s-wave photodetachment with $E_k \approx 0.1$ meV.	Discrete peaks if gap > 1 meV, be able to measure many photodetachment channels simultaneously.																																																																																																																																
Availability to an element with an unknown EA	Need to know a rough EA value in advance.	Need to know a rough EA value in advance.	Measure a rough EA value first, and then improve its accuracy.																																																																																																																																
Typical accuracy	0.001–1 meV	0.001–0.01 meV	0.01–0.1 meV																																																																																																																																
Dynamic range	~10 meV	~0.1 meV	A few eV																																																																																																																																
Immunity to interferences	Sensitive to unknown nonzero baselines and non-Wigner effects and tends to underestimate the measurement uncertainty.	Signal to noise ratio deteriorates due to interferences from other channels.	Strong immunity to interferences thanks to discrete peaks, be able to discriminate the EA channel from excited states and molecular species with the same mass.																																																																																																																																
Applicability	Main group elements and partial late transitional elements	Elements in main groups IIIA–VIIA	All elements																																																																																																																																
Elements with recommended EA values (in eV) ^a	<table> <tbody> <tr><td>Li</td><td>0.618049(22)</td></tr> <tr><td>B</td><td>0.279723(26)</td></tr> <tr><td>O</td><td>1.461112972(87)</td></tr> <tr><td>Na</td><td>0.547926(25)</td></tr> <tr><td>Al</td><td>0.43283(5)</td></tr> <tr><td>Cl</td><td>3.612725(28)</td></tr> <tr><td>K</td><td>0.501459(13)</td></tr> <tr><td>Ca</td><td>0.02455(10)</td></tr> <tr><td>Cu</td><td>1.23578(4)</td></tr> <tr><td>Br</td><td>3.363588(3)</td></tr> <tr><td>Rb</td><td>0.485916(21)</td></tr> <tr><td>Sr</td><td>0.05206(6)</td></tr> <tr><td>Rh</td><td>1.14289(20)</td></tr> <tr><td>Pd</td><td>0.56214(12)</td></tr> <tr><td>Ag</td><td>1.30447(2)</td></tr> <tr><td>In</td><td>0.38392(6)</td></tr> <tr><td>Sb</td><td>1.047401(19)</td></tr> <tr><td>Cs</td><td>0.471626(25)</td></tr> <tr><td>Ba</td><td>0.14462(6)</td></tr> <tr><td>Pt</td><td>2.12510(5)</td></tr> <tr><td>Au</td><td>2.30861(3)</td></tr> <tr><td>Tl</td><td>0.320053(19)</td></tr> <tr><td>Bi</td><td>0.942362(13)</td></tr> <tr><td>At</td><td>2.41578(7)</td></tr> </tbody> </table>	Li	0.618049(22)	B	0.279723(26)	O	1.461112972(87)	Na	0.547926(25)	Al	0.43283(5)	Cl	3.612725(28)	K	0.501459(13)	Ca	0.02455(10)	Cu	1.23578(4)	Br	3.363588(3)	Rb	0.485916(21)	Sr	0.05206(6)	Rh	1.14289(20)	Pd	0.56214(12)	Ag	1.30447(2)	In	0.38392(6)	Sb	1.047401(19)	Cs	0.471626(25)	Ba	0.14462(6)	Pt	2.12510(5)	Au	2.30861(3)	Tl	0.320053(19)	Bi	0.942362(13)	At	2.41578(7)	<table> <tbody> <tr><td>C</td><td>1.2621226(12)</td></tr> <tr><td>F</td><td>3.4011895(25)</td></tr> <tr><td>Si</td><td>1.3895212(7)</td></tr> <tr><td>P</td><td>0.746609(9)</td></tr> <tr><td>S</td><td>2.0771042(6)</td></tr> <tr><td>Ge</td><td>1.2326764(12)</td></tr> <tr><td>Se</td><td>2.0206047(11)</td></tr> <tr><td>Sn</td><td>1.112070(2)</td></tr> <tr><td>I</td><td>3.0590465(36)</td></tr> <tr><td>Pb</td><td>0.356721(2)</td></tr> </tbody> </table>	C	1.2621226(12)	F	3.4011895(25)	Si	1.3895212(7)	P	0.746609(9)	S	2.0771042(6)	Ge	1.2326764(12)	Se	2.0206047(11)	Sn	1.112070(2)	I	3.0590465(36)	Pb	0.356721(2)	<table> <tbody> <tr><td>Sc</td><td>0.179378(22)</td></tr> <tr><td>Ti</td><td>0.07554(5)</td></tr> <tr><td>V</td><td>0.52766(20)</td></tr> <tr><td>Cr</td><td>0.675928(27)</td></tr> <tr><td>Fe</td><td>0.153236(34)</td></tr> <tr><td>Co</td><td>0.662255(47)</td></tr> <tr><td>Ni</td><td>1.157368(58)</td></tr> <tr><td>Ga</td><td>0.301166(15)</td></tr> <tr><td>As</td><td>0.804485(6)</td></tr> <tr><td>Y</td><td>0.31129(22)</td></tr> <tr><td>Zr</td><td>0.433283(89)</td></tr> <tr><td>Nb</td><td>0.91740(7)</td></tr> <tr><td>Mo</td><td>0.74723(8)</td></tr> <tr><td>Ru</td><td>1.046270(20)</td></tr> <tr><td>Te</td><td>1.970861(9)</td></tr> <tr><td>La</td><td>0.557546(20)</td></tr> <tr><td>Ce</td><td>0.600160(26)</td></tr> <tr><td>Pr</td><td>0.10923(46)</td></tr> <tr><td>Nd</td><td>0.09748(31)</td></tr> <tr><td>Gd</td><td>0.212(30)</td></tr> <tr><td>Tb</td><td>0.13131(80)</td></tr> <tr><td>Lu</td><td>0.23882(62)</td></tr> <tr><td>Hf</td><td>0.1780(6)</td></tr> <tr><td>Ta</td><td>0.328859(22)</td></tr> <tr><td>W</td><td>0.816500(82)</td></tr> <tr><td>Re</td><td>0.060396(63)</td></tr> <tr><td>Os</td><td>1.077661(24)</td></tr> <tr><td>Ir</td><td>1.564057(11)</td></tr> <tr><td>Th</td><td>0.607690(60)</td></tr> <tr><td>U</td><td>0.31497(9)</td></tr> </tbody> </table>	Sc	0.179378(22)	Ti	0.07554(5)	V	0.52766(20)	Cr	0.675928(27)	Fe	0.153236(34)	Co	0.662255(47)	Ni	1.157368(58)	Ga	0.301166(15)	As	0.804485(6)	Y	0.31129(22)	Zr	0.433283(89)	Nb	0.91740(7)	Mo	0.74723(8)	Ru	1.046270(20)	Te	1.970861(9)	La	0.557546(20)	Ce	0.600160(26)	Pr	0.10923(46)	Nd	0.09748(31)	Gd	0.212(30)	Tb	0.13131(80)	Lu	0.23882(62)	Hf	0.1780(6)	Ta	0.328859(22)	W	0.816500(82)	Re	0.060396(63)	Os	1.077661(24)	Ir	1.564057(11)	Th	0.607690(60)	U	0.31497(9)
Li	0.618049(22)																																																																																																																																		
B	0.279723(26)																																																																																																																																		
O	1.461112972(87)																																																																																																																																		
Na	0.547926(25)																																																																																																																																		
Al	0.43283(5)																																																																																																																																		
Cl	3.612725(28)																																																																																																																																		
K	0.501459(13)																																																																																																																																		
Ca	0.02455(10)																																																																																																																																		
Cu	1.23578(4)																																																																																																																																		
Br	3.363588(3)																																																																																																																																		
Rb	0.485916(21)																																																																																																																																		
Sr	0.05206(6)																																																																																																																																		
Rh	1.14289(20)																																																																																																																																		
Pd	0.56214(12)																																																																																																																																		
Ag	1.30447(2)																																																																																																																																		
In	0.38392(6)																																																																																																																																		
Sb	1.047401(19)																																																																																																																																		
Cs	0.471626(25)																																																																																																																																		
Ba	0.14462(6)																																																																																																																																		
Pt	2.12510(5)																																																																																																																																		
Au	2.30861(3)																																																																																																																																		
Tl	0.320053(19)																																																																																																																																		
Bi	0.942362(13)																																																																																																																																		
At	2.41578(7)																																																																																																																																		
C	1.2621226(12)																																																																																																																																		
F	3.4011895(25)																																																																																																																																		
Si	1.3895212(7)																																																																																																																																		
P	0.746609(9)																																																																																																																																		
S	2.0771042(6)																																																																																																																																		
Ge	1.2326764(12)																																																																																																																																		
Se	2.0206047(11)																																																																																																																																		
Sn	1.112070(2)																																																																																																																																		
I	3.0590465(36)																																																																																																																																		
Pb	0.356721(2)																																																																																																																																		
Sc	0.179378(22)																																																																																																																																		
Ti	0.07554(5)																																																																																																																																		
V	0.52766(20)																																																																																																																																		
Cr	0.675928(27)																																																																																																																																		
Fe	0.153236(34)																																																																																																																																		
Co	0.662255(47)																																																																																																																																		
Ni	1.157368(58)																																																																																																																																		
Ga	0.301166(15)																																																																																																																																		
As	0.804485(6)																																																																																																																																		
Y	0.31129(22)																																																																																																																																		
Zr	0.433283(89)																																																																																																																																		
Nb	0.91740(7)																																																																																																																																		
Mo	0.74723(8)																																																																																																																																		
Ru	1.046270(20)																																																																																																																																		
Te	1.970861(9)																																																																																																																																		
La	0.557546(20)																																																																																																																																		
Ce	0.600160(26)																																																																																																																																		
Pr	0.10923(46)																																																																																																																																		
Nd	0.09748(31)																																																																																																																																		
Gd	0.212(30)																																																																																																																																		
Tb	0.13131(80)																																																																																																																																		
Lu	0.23882(62)																																																																																																																																		
Hf	0.1780(6)																																																																																																																																		
Ta	0.328859(22)																																																																																																																																		
W	0.816500(82)																																																																																																																																		
Re	0.060396(63)																																																																																																																																		
Os	1.077661(24)																																																																																																																																		
Ir	1.564057(11)																																																																																																																																		
Th	0.607690(60)																																																																																																																																		
U	0.31497(9)																																																																																																																																		

^a Recommended EA values for these elements are from our previous review [8] except the EA value of O from Ref.[49].

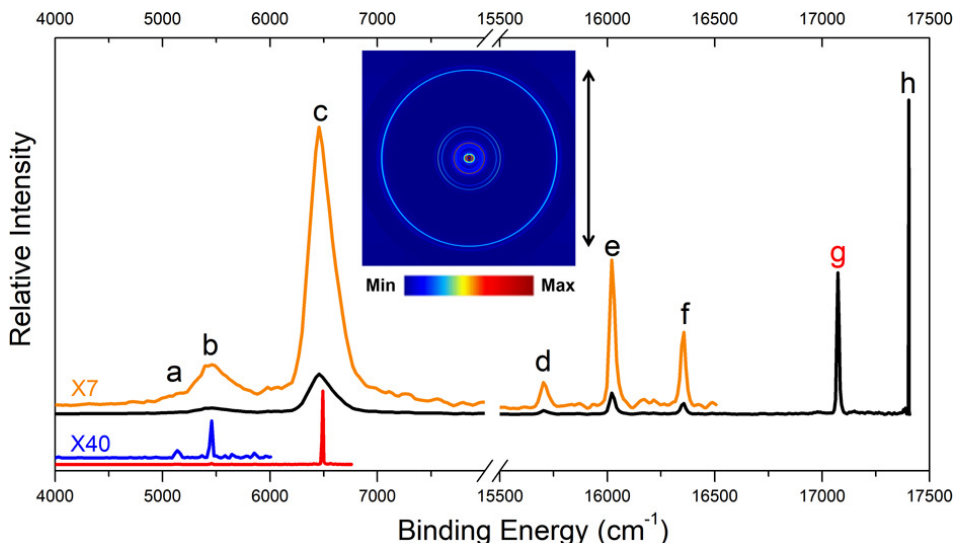


FIG. 4 Photoelectron spectra and image for As^- at photon energy $\hbar\nu=17407 \text{ cm}^{-1}$. The double arrow indicates the polarization of the photodetachment laser. The orange curve shows the weak peaks (a, b, c, d, e, and f) multiplied by a factor of 7. The red curve is the photoelectron spectra at photon energy $\hbar\nu=6757 \text{ cm}^{-1}$. The blue curve shows the weak peaks (a and b) multiplied by a factor of 40. Peak g is related to the transition $\text{As}^- (4s^24p^4\ ^3P_2) \rightarrow \text{As} (4s^24p^3\ ^2D_{3/2})$, which is used to measure the electron affinity of As in the present work.

linewidth ~ 0.06 cm $^{-1}$). In the present work, the ion trap temperature was maintained at 300 K, and the trap time was set to 45 ms. To accurately determine the binding energy of peaks a, b, and c, we further measured the spectra near the photodetachment threshold at photon energy $h\nu = 6757$ cm $^{-1}$ using an optical parametric oscillator (OPO) laser (Spectra-Physics primoScan, 400–2700 nm, linewidth ~ 6 cm $^{-1}$), as shown by red and blue curves in FIG. 4. A total of eight distinct peaks labelled a–h were successfully resolved, corresponding to different transitions from $4s^24p^4\ ^3P$ fine structure. The spectra measured using the OPO laser were employed to observe the overall features of photo-electron energy spectra and to obtain the preliminary values of the binding energies of peaks since the OPO laser has a convenience for tuning its wavelength. The dye laser with a narrow linewidth was used to further enhance the accuracy. The assignment of these peaks was supported by comparing the energy levels of neutral As atom obtained from the NIST database, which served as useful “fingerprints” for state identification [75]. The diagram in FIG. 5 illustrates these transitions. The assignment and binding energy of each peak are summarized in Table I. The first broad peak in FIG. 4 consists of two transitions: a and b, corresponding to the transition As $^4S_{3/2} \leftarrow$ As $^-$ 3P_0 and As $^4S_{3/2} \leftarrow$ As $^-$ 3P_1 , respectively. Peaks c, g, and h are all associated with the transitions from the ground state $4s^24p^4\ ^3P_2$ of

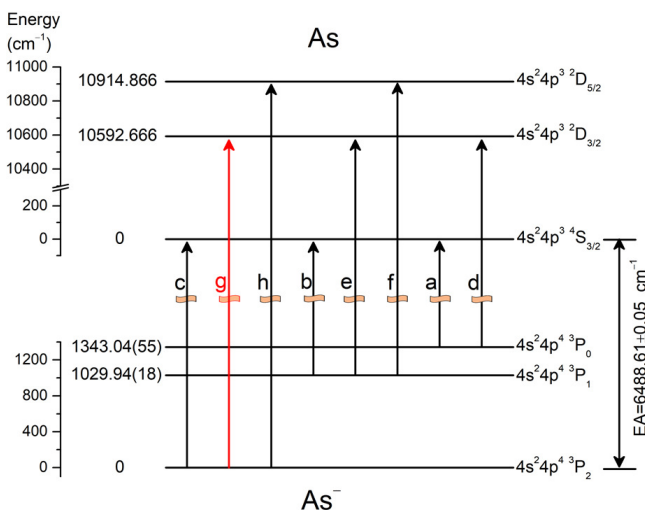


FIG. 5 Energy levels of As and As^- related to the present measurement. The ground state of As^- is $4s^24p^4\ 3P_2$. The ground state of As is $4s^24p^3\ 4S_{3/2}$. The labels of each transition are the same as the peaks observed in FIG. 4. Channel g marked in red is employed for the measurement of the electron affinity of As.

As^- . While in principle, any transition from the anionic ground state can be used to measure the EA value, the photon energy for the threshold photodetachment of peaks c is beyond the tuning range of our dye laser, and peak h is close to the dead zone of our dye laser. Consequently, we have chosen peak g, corresponding to the transition $\text{As}^- (4s^2 4p^4 3P_2) \rightarrow \text{As} (4s^2 4p^3 2D_{3/2})$, as the target channel for the EA measurement in this study.

To accurately determine the value of EA (As), a se-

TABLE II Measured binding energies and optimized binding energies of transitions observed in the present work.

Peak	Levels ($\text{As}^- \rightarrow \text{As}$)	Measured binding energy/ cm^{-1}	Optimized binding energy ^a / cm^{-1}
a	$4s^24p^4\ ^3P_0 \rightarrow 4s^24p^3\ ^4S_{3/2}$	5138.3(69)	5147.5(13)
b	$4s^24p^4\ ^3P_1 \rightarrow 4s^24p^3\ ^4S_{3/2}$	5451.3(70)	5458.54(15)
c	$4s^24p^4\ ^3P_2 \rightarrow 4s^24p^3\ ^4S_{3/2}$	6488.3(61)	6488.61(5)
d	$4s^24p^4\ ^3P_0 \rightarrow 4s^24p^3\ ^2D_{3/2}$	15740.5(13)	15740.2(13)
e	$4s^24p^4\ ^3P_1 \rightarrow 4s^24p^3\ ^2D_{3/2}$	16051.53(73)	16051.21(15)
f	$4s^24p^4\ ^3P_1 \rightarrow 4s^24p^3\ ^2D_{5/2}$	16373.40(15)	16373.41(15)
g	$4s^24p^4\ ^3P_2 \rightarrow 4s^24p^3\ ^2D_{3/2}$	17081.30(7)	17081.28(5)
h	$4s^24p^4\ ^3P_2 \rightarrow 4s^24p^3\ ^2D_{5/2}$	17403.45(7)	17403.47(5)

^a Deduced value according to the assignment, the measured EA value, the measured binding energy of peaks, and the energy levels of the neutral atom As.

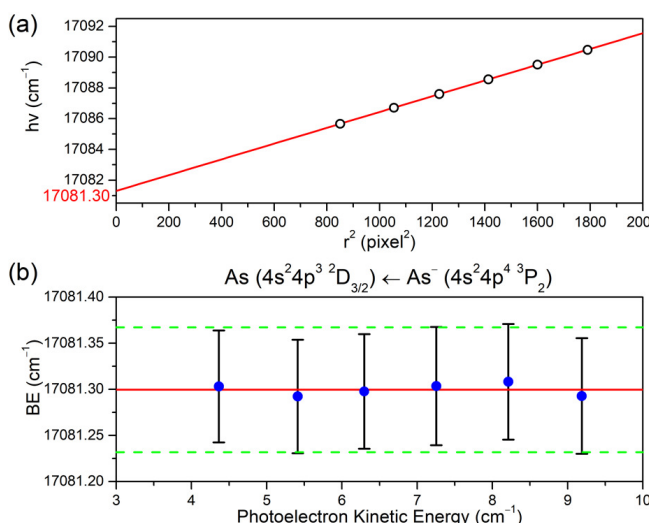


FIG. 6 (a) The photon energy $h\nu$ vs. the squared radius r^2 of the photoelectron spherical shell for transition g. The solid line is the linear least squares fitting. The intercept 17081.30(7) cm^{-1} is the binding energy of photodetachment channel g. (b) The binding energy of transition g as a function of the kinetic energy of photoelectrons. The dashed lines indicate the uncertainty of $\pm 0.07 \text{ cm}^{-1}$.

ries of spectra were measured near the threshold of peak g at the imaging voltage of -150 V. The photon energy was scanned from 17086 cm^{-1} to 17091 cm^{-1} with a step of 1 cm^{-1} , slightly above the threshold. Consequently, the kinetic energy E_k for channel g ranged from 4 cm^{-1} to 9 cm^{-1} . Since $h\nu = \text{BE} + \alpha r^2$, the experimental data were plotted as $h\nu$ vs. r^2 in FIG. 6(a), where r is the radius of the photoelectron shell of transition g, α is the slope, and the intercept of the fitted line indicates the binding energy (BE) of transition g, which was determined to be 17081.30 cm^{-1} with an uncertainty 0.07 cm^{-1} . FIG. 6(b) shows the binding energy of transition g measured at the different kinetic energy E_k . The uncertainty 0.07 cm^{-1} includes the contribution of the

laser line width 0.06 cm^{-1} . Since the final state of transition g, As ($4s^24p^3\ ^2D_{3/2}$), is 10592.666(12) cm^{-1} above the ground state of As [76], the preliminary EA value of As is determined to be 6488.63(7) cm^{-1} or 0.804488(9) eV by subtracting 10592.666 cm^{-1} from 17081.30 cm^{-1} . Considering the observation of multiple transitions, the EA value is further optimized to be 6488.61(5) cm^{-1} or 0.804485(6) eV via a global optimization analysis based on covariance algebra [10, 77, 78], which is consistent with the previously reported value of 0.8048(2) eV [79] but exhibits an improved accuracy by a factor of 30. It is worth noting that according to 2018 CODATA (committee on Data for Science and Technology), 1 eV = 8065.543937 cm^{-1} [80].

Peaks d, e, and f become very weak near their threshold due to the Wigner threshold law and the very low population on the excited states 3P_1 and 3P_0 . To accurately measure their energy level, a different technique was employed. The local linear interpolation method was utilized to determine the kinetic energy E_k using the equation:

$$E_k = E_{k0} + \alpha (r^2 - r_0^2), \quad (5)$$

where r is the radius of the peak to be determined, E_{k0} and r_0 correspond to the kinetic energy and the radius of a reference transition with a known accurate binding energy, and α is the energy calibration coefficient. This method reduces errors compared to the direct use of $E_k = \alpha r^2$ when $r \approx r_0$. In the present work, the transition g was chosen as the reference transition. To enhance peak f, the kinetic energy was increased to ~60 cm^{-1} . In Eq.(5), E_{k0} can be considered as an accurate value, as it is derived from $h\nu_0 - \text{BE}_0$, where $h\nu_0$ is monitored via a wavelength meter with an accuracy

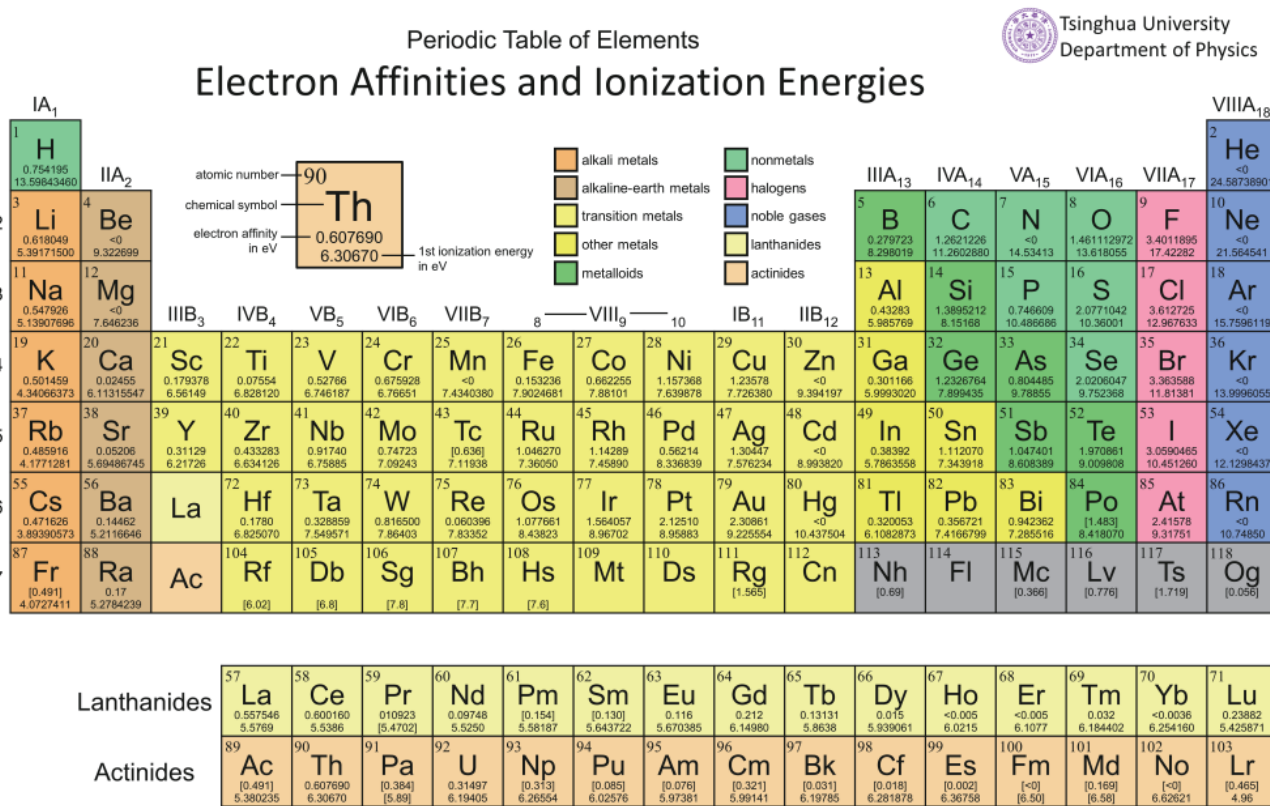


FIG. 7 Periodic table of elements with recommended electron affinities and first ionization energies. The values in brackets are theoretic results.

TABLE III Summary of the fine structures of As^- and the electron affinity results of As.

Reference	Fine structures of As^-		EA of As / eV
	$^3\text{P}_1 \leftarrow ^3\text{P}_2$	$^3\text{P}_0 \leftarrow ^3\text{P}_2$	
Ref.[92]		0.17	0.810(30)
Ref.[93]	0.125(3)	0.166(5)	
Ref.[94]	0.127(16)	0.161(16)	0.814(8)
Ref.[79]	0.1276(2)	0.1643(10)	0.8048(2)
This work	0.12770(3)	0.16652(7)	0.804485(6) ^a

^a 0.804485(6) eV=6488.61(5) cm⁻¹.

0.02 cm⁻¹ and the binding energy (BE_0) of transition g has been precisely measured as 17081.30(7) cm⁻¹. To accurately measure the binding energy of peak f, we tuned the photon energy $h\nu$ to make $r \approx r_0$. The radius r was determined through Gaussian function fitting, and the binding energy (BE) of transition f was deduced as $\text{BE} = h\nu - E_k$. The energy level of the fine-structure excited state $^3\text{P}_1$ was determined as 1029.94(18) cm⁻¹ or 0.12770(3) eV above the ground state $^3\text{P}_2$. Similarly, the energy level of another fine-structure excited state $^3\text{P}_0$ was measured as 1343.04(55) cm⁻¹ or 0.16652(7) eV above the ground state $^3\text{P}_2$.

The EA value and the fine structure levels reported in this work are summarized and compared with previous results in Table III. Our fine-structure results agree with Walter's measurement [79], but the accuracy is improved by a factor of 10. To further compare our SE-VI method with the LPT and LPM methods, the EA values of different isotope of Te were also measured as $\text{EA}^{(130)\text{Te}} = 15896.07(7)$ cm⁻¹, $\text{EA}^{(128)\text{Te}} = 15896.02(8)$ cm⁻¹, and $\text{EA}^{(126)\text{Te}} = 15896.05(7)$ cm⁻¹, respectively. These values show marginal agreement with $\text{EA}^{(130)\text{Te}} = 15896.18(5)$ cm⁻¹ reported by Haefliger *et al.* using the LPT method [81]. Furthermore, we previously also measured the EA values of S [59], Pb [82], and I [59]. The EA(S) was measured as 16753.00(7) cm⁻¹ using our second-generation apparatus, which agrees excellently with the result 16752.9753(41) cm⁻¹ obtained using the LPM method [83]. The EA values of Pb and I were measured on our first generation apparatus, yielding $\text{EA}^{(208)\text{Pb}} = 2877.33(13)$ and $\text{EA}(\text{I}) = 24672.94(10)$ cm⁻¹. These values are consistent with previous measurements from Blondel group using the LPM method, except for a slight difference in the SEVI result of ^{208}Pb compared to their isotope-averaged result. Blondel group reported $\text{EA}(\text{I}) =$

24672.874(29) cm⁻¹ [84] and the isotope-averaged result of 2877.149(15) cm⁻¹ for Pb [85]. To investigate the reason for the discrepancy, the EA value of Pb was re-measured on our second-generation spectrometer. The newly obtained EA(²⁰⁸Pb)=2877.14(9) cm⁻¹ agrees with the recent measurement EA(²⁰⁸Pb)=2877.18(6) cm⁻¹ by Walter *et al.* using the LPT method [86] and the previous LPM result. Compared with our first-generation spectrometer, the key difference for the new apparatus is the ion trap, which decouples the ion beam from the fluctuation of the laser-ablation ion source, contributing to better stability of the intersection point of the ion beam and photodetachment laser beam. Moreover, a new phosphor screen with a higher gain is used. The energy resolution of our new spectrometer was improved with the aforementioned measures.

In FIG. 7, we provide a convenient reference for readers by listing the recommended electron affinity and the first ionization energy in the periodic table of elements. The recommended EA values are primarily from our previous review published in the Journal of Physical and Chemical Reference Data, titled “Electron Affinities of Atoms and Structures of Atomic Negative Ions” [8]. The recommended first-ionization-energy values, on the other hand, are sourced from NIST Standard Reference Database 78, Version 5.10, 2022 [75]. This database is maintained by the National Institute of Standards and Technology (NIST) and provides authoritative and accurate reference data for scientific measurements [87]. These accurate experimental EA values and fine structures of atomic anions can serve as a reliable benchmark for developing more advanced theoretical calculations.

IV. CONCLUSION

In conclusion, we have compared three commonly used experimental methods for determining electron affinities, namely the slow electron velocity-map imaging method (SEVI), the laser photodetachment threshold method (LPT), and the laser photodetachment microscopy (LPM). We have highlighted the respective advantages and disadvantages of each method. To demonstrate the capabilities of the SEVI method employed in our study, we measured the electron affinity (EA) of As and the fine-structure states of As⁻. Our results revealed that EA(As) is 6488.61(5) cm⁻¹ or 0.804485(6) eV, and determined the fine-structure energy levels of As⁻ to be 1029.94(18) cm⁻¹ or 0.12770(3) eV

for ³P₁ and 1343.04(55) cm⁻¹ or 0.16652(7) eV for ³P₀ above the ground state ³P₂, respectively. The SEVI method, with its high energy resolution and a large dynamic range for photoelectron kinetic energy, offers a distinct advantage over LPT and LPM when studying atomic anions with complex structures. It enables precise investigations into the properties of all elements, and has been utilized to measure molecular ions [88–91].

V. ACKNOWLEDGMENTS

This work was supported by the National Natural Science Foundation of China (No.11974199 and No.91736102) and the National Key R&D Program of China (No.2018YFA0306504).

- [1] H. Hotop and W. C. Lineberger, *J. Phys. Chem. Ref. Data* **4**, 539 (1975).
- [2] H. Hotop and W. C. Lineberger, *J. Phys. Chem. Ref. Data* **14**, 731 (1985).
- [3] T. Andersen, H. K. Haugen, and H. Hotop, *J. Phys. Chem. Ref. Data* **28**, 1511 (1999).
- [4] J. C. Rienstra-Kiracofe, G. S. Tschumper, H. F. Schaefer, S. Nandi, and G. B. Ellison, *Chem. Rev.* **102**, 231 (2002).
- [5] T. Andersen, *Phys. Rep.* **394**, 157 (2004).
- [6] W. C. Lineberger, *Annu. Rev. Phys. Chem.* **64**, 21 (2013).
- [7] C. Blondel, C. Delsart, and F. Dulieu, *Phys. Rev. Lett.* **77**, 3755 (1996).
- [8] C. G. Ning, and Y. Z. Lu, *J. Phys. Chem. Ref. Data* **51**, 021502 (2022).
- [9] C. W. Walter, N. D. Gibson, R. L. Field, A. P. Sneden, J. Z. Shapiro, C. M. Janczak, and D. Hanstorp, *Phys. Rev. A* **80**, 014501 (2009).
- [10] R. J. Peláez, C. Blondel, M. Vandevraye, C. Drag, and C. Delsart, *J. Phys. B: Atom. Mol. Opt. Phys.* **44**, 195009 (2011).
- [11] M. Scheer, H. K. Haugen, and D. R. Beck, *Phys. Rev. Lett.* **79**, 4104 (1997).
- [12] R. C. Bilodeau and H. K. Haugen, *Phys. Rev. A* **64**, 024501 (2001).
- [13] P. Kristensen, U. V. Pedersen, V. V. Petrunin, T. Andersen, and K. T. Chung, *Phys. Rev. A* **55**, 978 (1997).
- [14] P. Kristensen, U. V. Pedersen, V. V. Petrunin, T. Andersen, and K. T. Chung, *Phys. Rev. A* **56**, 1674 (1997).
- [15] L. M. Blau, R. Novick, and D. Weinflash, *Phys. Rev. Lett.* **24**, 1268 (1970).
- [16] T. Andersen, L. H. Andersen, P. Balling, H. K. Hau-

- gen, P. Hvelplund, W. W. Smith, and K. Taulbjerg, *Phys. Rev. A* **47**, 890 (1993).
- [17] S. J. Buckma and C. W. Clark, *Rev. Mod. Phys.* **66**, 539 (1994).
- [18] C. W. Walter, J. A. Seifert, and J. R. Peterson, *Phys. Rev. A* **50**, 2257 (1994).
- [19] U. V. Pedersen, M. Hyde, S. P. Møller, and T. Andersen, *Phys. Rev. A* **64**, 012503 (2001).
- [20] A. Wolf, K. G. Bhushan, I. Ben-Itzhak, N. Altstein, D. Zajfman, O. Heber, and M. L. Rappaport, *Phys. Rev. A* **59**, 267 (1999).
- [21] G. Miecznik, T. Brage, and C. Froese Fischer, *Phys. Rev. A* **47**, 3718 (1993).
- [22] F. R. Simpson, R. Browning, and H. B. Gilbody, *J. Phys. B: Atom. Mol. Phys.* **4**, 106 (1971).
- [23] T. Brage and C. F. Fischer, *Phys. Rev. A* **44**, 72 (1991).
- [24] J. B. Fenn, M. Mann, C. K. Meng, S. F. Wong, and C. M. Whitehouse, *Science* **246**, 64 (1989).
- [25] R. Middleton, *Nucl. Instrum. Methods Phys. Res.* **214**, 139 (1983).
- [26] V. V. Petrunin, H. H. Andersen, P. Balling, and T. Andersen, *Phys. Rev. Lett.* **76**, 744 (1996).
- [27] H. H. Andersen, V. V. Petrunin, P. Kristensen, and T. Andersen, *Phys. Rev. A* **55**, 3247 (1997).
- [28] R. Zhang, Y. Z. Lu, R. L. Tang, and C. G. Ning, *J. Chem. Phys.* **158**, 084303 (2023).
- [29] R. L. Tang, X. X. Fu, and C. G. Ning, *J. Chem. Phys.* **149**, 134304 (2018).
- [30] X. X. Fu, Z. H. Luo, X. L. Chen, J. M. Li, and C. G. Ning, *J. Chem. Phys.* **145**, 164307 (2016).
- [31] S. Li, X. X. Fu, X. L. Chen, Y. Z. Lu, and C. G. Ning, *J. Chem. Phys.* **157**, 044302 (2022).
- [32] X. L. Chen, Z. H. Luo, J. M. Li, and C. G. Ning, *Sci. Rep.* **6**, 24996 (2016).
- [33] X. L. Chen and C. G. Ning, *Phys. Rev. A* **93**, 052508 (2016).
- [34] X. X. Fu, J. M. Li, Z. H. Luo, X. L. Chen, and C. G. Ning, *J. Chem. Phys.* **147**, 064306 (2017).
- [35] Z. H. Luo, X. L. Chen, J. M. Li, and C. G. Ning, *Phys. Rev. A* **93**, 020501 (2016).
- [36] R. L. Tang, X. L. Chen, X. X. Fu, H. Wang, and C. G. Ning, *Phys. Rev. A* **98**, 020501 (2018).
- [37] X. L. Chen and C. G. Ning, *J. Phys. Chem. Lett.* **8**, 2735 (2017).
- [38] Y. Z. Lu, J. Zhao, R. L. Tang, X. X. Fu, and C. G. Ning, *J. Chem. Phys.* **152**, 034302 (2020).
- [39] Y. Z. Lu, R. L. Tang, X. X. Fu, and C. G. Ning, *Phys. Rev. A* **99**, 062507 (2019).
- [40] X. X. Fu, R. L. Tang, Y. Z. Lu, and C. G. Ning, *Chin. Phys. B* **29**, 073201 (2020).
- [41] X. X. Fu, Y. Z. Lu, R. L. Tang, and C. G. Ning, *Phys. Rev. A* **101**, 022502 (2020).
- [42] X. X. Fu, R. L. Tang, Y. Z. Lu, and C. G. Ning, *Chin. J. Chem. Phys.* **32**, 187 (2019).
- [43] R. L. Tang, R. Si, Z. J. Fei, X. X. Fu, Y. Z. Lu, T. Brage, H. T. Liu, C. Y. Chen, and C. G. Ning, *Phys. Rev. Lett.* **123**, 203002 (2019).
- [44] R. L. Tang, R. Si, Z. J. Fei, X. X. Fu, Y. Z. Lu, T. Brage, H. T. Liu, C. Y. Chen, and C. G. Ning, *Phys. Rev. A* **103**, 042817 (2021).
- [45] R. L. Tang, Y. Z. Lu, H. T. Liu, and C. G. Ning, *Phys. Rev. A* **103**, L050801 (2021).
- [46] R. S. Berry, J. C. Mackie, R. L. Taylor, and R. Lynch, *J. Chem. Phys.* **43**, 3067 (2004).
- [47] W. C. Lineberger and B. W. Woodward, *Phys. Rev. Lett.* **25**, 424 (1970).
- [48] E. P. Wigner, *Phys. Rev.* **73**, 1002 (1948).
- [49] M. K. Kristiansson, K. Chartkunchand, G. Eklund, O. M. Hole, E. K. Anderson, N. de Ruette, M. Kamińska, N. Punnakayathil, J. E. Navarro-Navarrete, S. Sigurdsson, J. Grumer, A. Simonsson, M. Björkhage, S. Rosén, P. Reinhed, M. Blom, A. Källberg, J. D. Alexander, H. Cederquist, H. Zettergren, H. T. Schmidt, and D. Hanstorp, *Nat. Commun.* **13**, 5906 (2022).
- [50] C. Blondel, C. Delsart, F. Dulieu, and C. Valli, *Eur. Phys. J. D* **5**, 207 (1999).
- [51] C. Blondel, S. Berge, and C. Delsart, *Am. J. Phys.* **69**, 810 (2001).
- [52] C. Delsart, F. Goldfarb, and C. Blondel, *Phys. Rev. Lett.* **89**, 183002 (2002).
- [53] C. Blondel, W. Chaibi, C. Delsart, C. Drag, F. Goldfarb, and S. Kröger, *Eur. Phys. J. D* **33**, 335 (2005).
- [54] W. Chaibi, C. Blondel, C. Delsart, and C. Drag, *Europhys. Lett.* **82**, 20005 (2008).
- [55] A. T. J. B. Eppink and D. H. Parker, *Rev. Sci. Instrum.* **68**, 3477 (1997).
- [56] A. Osterwalder, M. J. Nee, J. Zhou, and D. M. Neumark, *J. Chem. Phys.* **121**, 6317 (2004).
- [57] D. M. Neumark, *J. Phys. Chem. A* **112**, 13287 (2008).
- [58] I. León, Z. Yang, H. T. Liu, and L. S. Wang, *Rev. Sci. Instrum.* **85**, 083106 (2014).
- [59] R. Tang, X. Fu, Y. Lu, and C. Ning, *J. Chem. Phys.* **152**, 114303 (2020).
- [60] W. C. Wiley and I. H. McLaren, *Rev. Sci. Instrum.* **26**, 1150 (1955).
- [61] W. A. de Heer and P. Milani, *Rev. Sci. Instrum.* **62**, 670 (1991).
- [62] C. N. Yang, *Phys. Rev.* **74**, 764 (1948).
- [63] J. Cooper and R. N. Zare, *J. Chem. Phys.* **48**, 942 (2003).
- [64] J. Cooper and R. N. Zare, *J. Chem. Phys.* **49**, 4252 (1968).
- [65] D. Hanstorp, C. Bengtsson, and D. J. Larson, *Phys. Rev. A* **40**, 670 (1989).
- [66] C. M. Oana and A. I. Krylov, *J. Chem. Phys.* **131**, 124114 (2009).
- [67] A. Sanov, *Annu. Rev. Phys. Chem.* **65**, 341 (2014).
- [68] Y. Liu and C. G. Ning, *J. Chem. Phys.* **143**, 144310

- (2015).
- [69] V. Dribinski, A. Ossadtchi, V. A. Mandelshtam, and H. Reisler, *Rev. Sci. Instrum.* **73**, 2634 (2002).
- [70] G. A. Garcia, L. Nahon, and I. Powis, *Rev. Sci. Instrum.* **75**, 4989 (2004).
- [71] B. Dick, *Phys. Chem. Chem. Phys.* **16**, 570 (2014).
- [72] B. Dick, *Phys. Chem. Chem. Phys.* **21**, 19499 (2019).
- [73] R. C. Bilodeau and H. K. Haugen, *Phys. Rev. Lett.* **85**, 534 (2000).
- [74] Y. Lu, R. Zhang, C. Song, C. Chen, R. Si, and C. Ning, *Chin. Phys. Lett.*, **40**, 093101 (2023).
- [75] J. E. Sansonetti, and W. C. Martin, *J. Phys. Chem. Ref. Data* **34**, 1559 (2005).
- [76] L. E. Howard and K. L. Andrew, *J. Opt. Soc. Am. B* **2**, 1032 (1985).
- [77] A. E. Kramida, *Comput. Phys. Commun.* **182**, 419 (2011).
- [78] L. J. Radziemski, K. J. Fisher, D. W. Steinhause, and A. S. Goldman, *Comput. Phys. Commun.* **3**, 9 (1972).
- [79] C. W. Walter, N. D. Gibson, R. L. Field, A. P. Sneden, J. Z. Shapiro, C. M. Janczak, and D. Hanstorp, *Phys. Rev. A* **80**, 014501 (2009).
- [80] E. Tiesinga, P. J. Mohr, D. B. Newell, and B. N. Taylor, *The 2018 CODATA Recommended Values of the Fundamental Physical Constants*, In: <http://physics.nist.gov/constants>.
- [81] G. Haeffler, A. E. Klinkmüller, J. Rangell, U. Berzinsh, and D. Hanstorp, *Z. Phys. D: At. Mol. Clusters* **38**, 211 (1996).
- [82] X. L. Chen and C. G. Ning, *J. Chem. Phys.* **145**, 084303 (2016).
- [83] T. Carette, C. Drag, O. Scharf, C. Blondel, C. Delsart, C. Froese Fischer, and M. Godefroid, *Phys. Rev. A* **81**, 042522 (2010).
- [84] R. J. Peláez, C. Blondel, C. Delsart, and C. Drag, *J. Phys. B: At. Mol. Opt. Phys.* **42**, 125001 (2009).
- [85] D. Bresteau, C. Drag, and C. Blondel, *J. Phys. B: At. Mol. Opt. Phys.* **52**, 065001 (2019).
- [86] C. W. Walter, F. E. Vassallo, and N. D. Gibson, *Phys. Rev. A* **106**, L010801 (2022).
- [87] A. Kramida, Y. Ralchenko, J. Reader, and NIST ASD Team (2022), In: NIST Atomic Spectra Database (version 5.10), [Online]. Available at <https://physics.nist.gov/asd> [Tue Jul 18 2023]. National Institute of Standards and Technology, Gaithersburg, MD. DOI: <https://doi.org/10.18434/T4W30F>.
- [88] Y. Z. Lu, R. L. Tang, R. Zhang, and C. G. Ning, *J. Phys. Chem. Lett.* **13**, 8711 (2022).
- [89] Y. Z. Lu and C. G. Ning, *J. Phys. Chem. Lett.* **13**, 4995 (2022).
- [90] Y. Z. Lu, R. L. Tang, X. X. Fu, H. T. Liu, and C. G. Ning, *J. Chem. Phys.* **154**, 074303 (2021).
- [91] Y. T. Wang, C. G. Ning, H. T. Liu, and L. S. Wang, *J. Phys. Chem. A* **124**, 5720 (2020).
- [92] D. Feldmann, R. Rackwitz, E. Heinicke, and H. J. Kaiser, *Z. Phys. A* **282**, 143 (1977).
- [93] G. Haeffler, U. Ljungblad, I. Y. Kiyan, and D. Hanstorp, *Z. Phys. D: At. Mol. Clusters* **42**, 263 (1997).
- [94] T. P. Lippa, S. J. Xu, S. A. Lyapustina, J. M. Nilles, and K. H. Bowen, *J. Chem. Phys.* **109**, 10727 (1998).